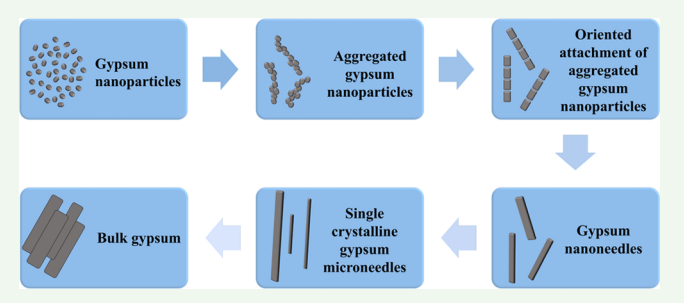
www.acsanm.org

In Situ Transmission Electron Microscopy Explores a New Nanoscale Pathway for Direct Gypsum Formation in Aqueous Solution

Kun He, $^{\dagger, \ddagger, \parallel}$ Anmin Nie, $^{\$, \nabla_{\bullet}}$ Yifei Yuan, $^{\ddagger, \parallel}$ Seyed Mohammadreza Ghodsi, $^{\bot_{\bullet}}$ Boao Song, $^{\ddagger_{\bullet}}$ Emre Firlar, $^{\ddagger, \bot}$ Jun Lu, $^{\parallel_{\bullet}}$ Yu-peng Lu, $^{\dagger, \parallel}$ Tolou Shokuhfar, $^{*, \bot}$ Constantine M. Megaridis, $^{*, \ddagger_{\bullet}}$ and Reza Shahbazian-Yassar*,‡

Supporting Information

ABSTRACT: In the modern construction industry, large gypsum (CaSO₄·2H₂O) boards are manufactured through a two-step procedure, which features the heating of fine gypsum powders to form the intermediate plaster of Paris (bassanite, CaSO₄·0.5H₂O) followed by hydration of the intermediate phase to form the final formed product. Here, we explore a novel pathway toward the fabrication of gypsum microneedles that bypasses formation of the intermediate bassanite phase. Using in situ liquid transmission electron microscopy, the dynamic behavior of fine gypsum powders in a calcium sulfate



solution is investigated at the nanoscale and in real time. An oriented-attachment mechanism is found to dominate the direct transformation of gypsum nanoparticles to gypsum microneedles, where no intermediate phases are involved. Our experimental results advance the fundamental understanding of the dynamic interactions between gypsum and water. The proposed nanoscale pathway for gypsum evolution could potentially revolutionize the construction industry rooted in gypsum board manufacturing by promising a time- and energy-efficient mass production procedure. In addition, this work can inspire research efforts associated with geology, archeology, and biology, where historical significance is frequently deduced from gypsum-related

KEYWORDS: liquid cell microscopy, transmission electron microscopy, gypsum, bassanite, calcium sulfate

1. INTRODUCTION

Calcium sulfate (CaSO₄) is an abundant mineral in the Earth's crust and can be found in sand, mineral deposits, and seawater.² This material has attracted substantial attention because of its wide applications in geology, 3,4 archeology, 5,6 medical devices, ^{7,8} infrastructure, ⁹⁻¹¹ and surgical training. ¹² Most CaSO₄ applications are typically based on complicated interactions among various phases in aqueous solutions, such as calcium sulfate dihydrate (CaSO₄·2H₂O, also known as gypsum), calcium sulfate hemihydrate (CaSO₄·0.5H₂O, also known as bassanite), and calcium sulfate anhydrite (CaSO₄). Among all of these polymorphs, gypsum is the most stable in the atmosphere and is thus the dominant phase in most applications. The formation of gypsum is believed to start with Ca²⁺ and SO₄²⁻ supersaturation within an aqueous solution and then proceed via the nucleation of bassanite, followed by particle aggregation and a subsequent phase transition to gypsum. 13,14 Current mass production of gypsum plaster largely relies on this multistep reaction and particularly requires the calcination of ground gypsum at 150-165 °C to form bassanite. 15,16 Such a phase transition is always plagued by the high energy barrier associated with the multistep kinetics, which inevitably results in extra cost and time devoted to the mass production of gypsum. As such, numerous efforts have been spent investigating the fundamentals of gypsum evolution during its precipitation and dissolution in different aqueous environments, such as seawater, brine in basin, 17 and scaling water. 18

Transmission electron microscopy (TEM) is a powerful technique that has been previously used to investigate gypsum

Received: May 3, 2018 Accepted: September 27, 2018 Published: September 27, 2018



 $^{^\}dagger$ School of Materials Science and Engineering and ¶ Key Laboratory for Liquid–Solid Structural Evolution and Processing of Materials, Ministry of Education, Shandong University, Ji'nan 250000, China

 $^{^{\}ddagger}$ Department of Mechanical and Industrial Engineering and $^{\perp}$ Department of Bioengineering, University of Illinois at Chicago, Chicago, Illinois 60607, United States

[§]Materials Genome Institute, Shanghai University, 99 Shangda Road, Shanghai 200444, China

Chemical Science and Engineering Division, Argonne National Laboratory, Argonne, Illinois 60639, United States

[∇]State Key Laboratory of Metastable Materials Science and Technology, Yanshan University, Qinhuangdao 066004, China

ACS Applied Nano Materials Article

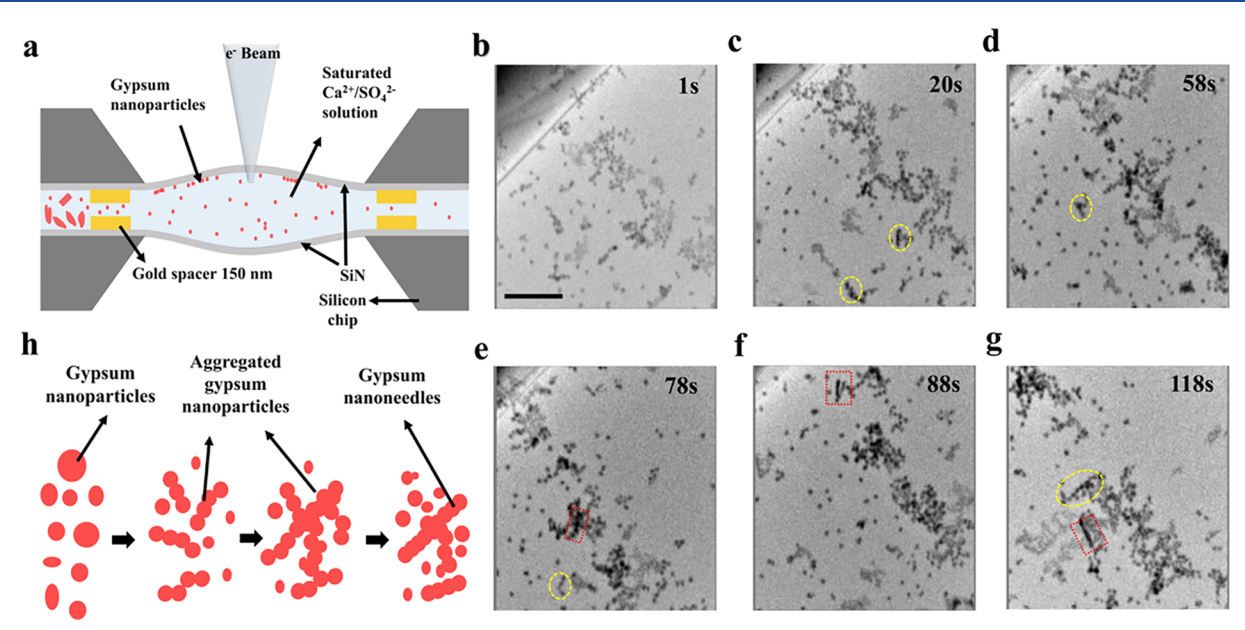


Figure 1. (a) Schematic of the in situ liquid-cell TEM setup used to observe the growth of gypsum nanoparticles in an aqueous solution. (b–g) Time-sequential TEM images showing how gypsum nanoparticles aggregate and form gypsum nanoneedles in a SO_4^{2-} - and Ca^{2+} -saturated aqueous solution in a liquid cell. Gypsum nanoneedle formation occurs in two stages: (b–d) Aggregation of preexisting gypsum nanoparticles; (e–g) TEM snapshots of the transformation of agglomerated nanoparticles to gypsum nanoneedles. The scale bar in part b applies to parts b–g and denotes 1 μ m. The electron dose rate for all of these images was 798 e nm⁻² s⁻¹. (h) Schematic depiction of the aggregation process of gypsum nanoparticles toward the needle morphology.

evolution in aqueous solutions. Wang et al.13 explored the precipitation process of gypsum by observing the mixing products of calcium and sulfate solutions in conventional (vacuum) TEM. They suggested that the route featured the formation of amorphous CaSO₄, which was converted to bassanite crystals and eventually to gypsum. Using time-resolved cryo-TEM, Van Driessche et al. 14 demonstrated that single-crystalline bassanite functioned as a stable precursor during the precipitation of gypsum needles by the mixing of CaCl₂·2H₂O and Na₂SO₄ solutions. The precipitation of gypsum in water was also reported to be a hydration process, during which the nanoscale amorphous cluster first evolved to amorphous particles and then transformed to crystalline needle-shaped gypsum. 19 Using synchrotron X-ray (smalland wide-angle scattering) techniques, gypsum was also found to form by the aggregation and rearrangement of sub-3-nm anhydrated particles.²⁰ The crystallization pathways of gypsum precipitation were also explored by Raman and IR spectroscopy, ^{21,22} where a nonclassical nucleation theory involving an amorphous phase and other CaSO₄ polymorphs was proposed. Yet, there has been no reliable and direct in situ evidence regarding the reaction kinetics and identification of the various phases involved.

Despite various ex situ studies devoted to the understanding of gypsum formation 13,14,17,20-24 and dissolution, 1,3,25 the fundamentals of dynamic phase transition and morphology evolution in this process have not been fully understood. Herein, for the first time, in situ liquid-cell TEM is utilized to observe the evolution of gypsum nanoparticles in aqueous solutions in real time. Liquid-cell TEM has undergone rapid development in recent years and thus has become a powerful tool for exploring biological and material science processes in real time and with nanoscale resolution. 26-30 When selected liquids are forced through the cells (flow mode), material behaviors such as nanoparticle movement 31,27,32,33 and lithium

dendrite growth during battery cycling^{34,35} have been intensively studied. We report here a new mechanism accounting for the gypsum formation process, which coexists with the conventional phase-transition pathway. Arguments are provided and discussed in detail based on real-time observations of gypsum evolution in aqueous solutions. This new transition route is found to successfully circumvent the notorious energy barriers plaguing the traditional phasetransition pathways and demonstrated as a novel and efficient strategy to control the gypsum evolution. The present work advances the fundamental understanding of gypsum behavior in water and thus can inspire future research in the fields of geology, archeology, and biology, where gypsum-related discoveries are highly relevant. More importantly, the construction industry sectors rooted in CaSO₄ compounds can potentially benefit from these findings through proper adjustment of the material processing technology toward a more time- and cost-effective mass production.

2. EXPERIMENTAL SECTION

2.1. Materials. The gypsum powder was provided by USG. The corresponding X-ray diffraction (XRD) pattern is shown in Figure S1a and confirms that the powders are pure calcium sulfate dihydrate (CaSO₄·2H₂O) according to the standard XRD data (PDF 00-033-0311). Parts b and c of Figure S1 show respectively low- and highmagnification TEM images, revealing the morphology of the asreceived gypsum particles, which have various shapes with sizes ranging from nanometers to micrometers. No needle-shaped particles were observed in the as-received powder. Rather, the gypsum particles looked like stacked flakes. Electron energy loss spectroscopy and energy-dispersive spectroscopy data confirmed the presence of Ca, O, and S elements in the sample. On the basis of the atomic models of bassanite and gypsum (parts f and g of Figure S1, respectively), one can see how the different amounts of bonded water cause structure change. Gypsum can be distinguished from bassanite by means of the XRD pattern.

ACS Applied Nano Materials Article

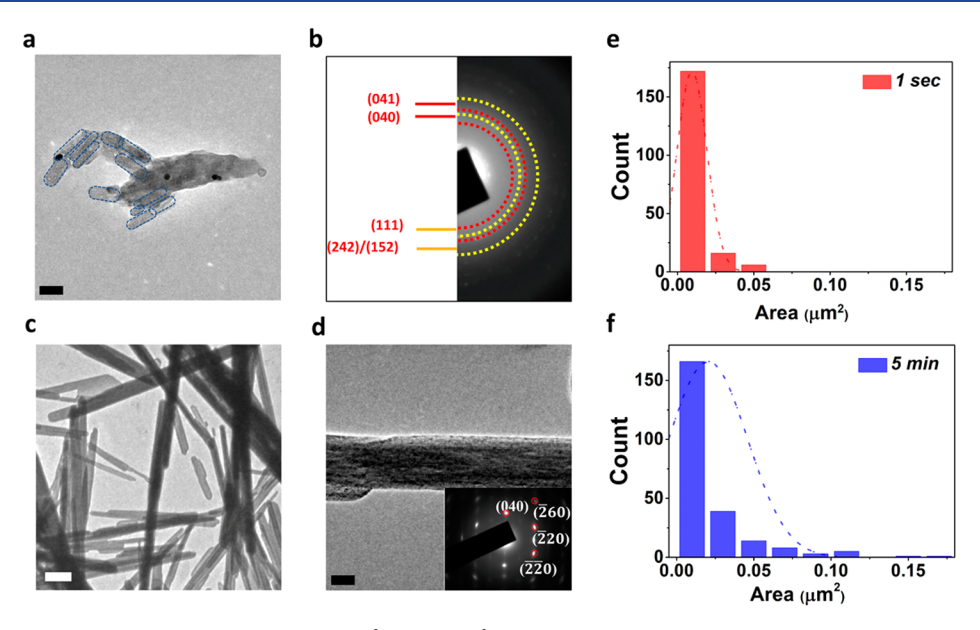


Figure 2. TEM characterization of gypsum exposed to a Ca²⁺- and SO₄²⁻-saturated aqueous solution: (a and b) formation of aggregated gypsum nanoparticles after 5 min of exposure; (c, d) formation of gypsum microneedles after 30 min of exposure. The scale bars in parts a, c, and d denote 50, 500, and 100 nm, respectively. (b) Selected-Area Electron Diffraction (SAED) pattern from the large particles shown in part a, which is confirmed to be monoclinic gypsum by the appearance of the characteristic diffraction rings. The inset image in part d is the SAED pattern of the shown gypsum nanoneedle viewed along the [001] zone axis, and confirms a typical single-crystal diffraction pattern. (e) Histogram of the projected particle area obtained in Figure 1 b, i.e., after 1 s exposure time. (f) Histogram of the projected particle area obtained from 35 images of samples with 5 min exposure time.

2.2. XRD Characterization. A Siemens (Bruker) D-5000 powder diffractometer (equipped with a standard sample holder) was used to detect the composition of the as-received dry powder. The diffractometer uses Cu Clpha radiation with a 0.02 $^\circ$ step size and a 2 s dwell time.

2.3. Preparation of In Situ Liquid-Cell Experiments. All in situ liquid-cell experiments were carried out using the Protochips Poseidon 500 liquid holder in an aberration-corrected JEOL JEM-ARM 200CF scanning transmission electron microscope operated at 200 kV in TEM mode. The design of the tip of the holder can be seen in Figure 1a. The chip spacers used in the experiments were 150 nm (the top and bottom windows were separated by this distance). For Movie S1 and Figures 1 and 2, the ground gypsum nanoparticles were dispersed in isopropyl alcohol (IPA) and sonicated for 5 min. Then the gypsum dispersion was driven into the liquid cell. After the cell was filled with the fluid, air flow was initiated and maintained for 40 min to purge all IPA (but not the particles, which stayed in the cell) from the cell chamber. At that point, the flow of a Ca²⁺- and SO₄²⁻saturated solution into the chamber was initiated and maintained for the duration of the test. For Movie S1 (Figure 1), the beam was stopped only during the purging air flow. For Figure 2, the sample was not inserted into the microscope (thus providing a control case). These samples were harvested at 5 and 30 min. The silicon nitride chips were opened to perform ex situ characterization after loading in the TEM. For Movie S2 and Figure 3, the gypsum particles were loaded into the chip (with 500 nm spacers) before assembly. Deionized water was forced into the cell until a droplet could be seen to emerge from the outlet of the holder, at which time the flow was stopped. Movie S3 and Figure S5 were captured during a 30 min period after the flow was stopped. For Movie S4 and Figure 4, the Ca2+- and SO42--saturated solution was forced through the cell, and once fluid emerged from the outlet of the holder, the flow was stopped.

3. RESULTS AND DISCUSSION

3.1. Aggregation of Gypsum Nanoparticles. To observe the interaction of pristine gypsum nanoparticles (Figure S1) with water, the particles were preloaded into the liquid cell using the experimental scheme illustrated in Figure 1a. The sample preparation is explained in the Supporting Information. We studied the evolution of gypsum nanoparticles in an aqueous solution saturated with sulfate (SO₄²⁻) and calcium (Ca2+) ions by liquid-cell TEM. As shown in Table S1, the concentrations of the SO₄²⁻ and Ca²⁺ ions were maintained above the solubility limit of gypsum in water (15.7 mM) in order to prevent dissolution of the existing or newly formed gypsum nanoparticles. Parts b-g of Figure 1 elucidate the detailed formation process of gypsum nanoneedles starting from the preloaded gypsum nanoparticles. Figure 1b shows that the gypsum nanoparticles are well dispersed in the saturated solution, while they tend to be concentrated in several locations where they appear as aggregated clusters. Parts c and d of Figure 1 capture the gradual attachment of gypsum nanoparticles, which results in the appearance of newly aggregated gypsum nanoparticles (yellow-dotted circles). At later stages, the aggregated gypsum nanoparticles grow into even larger nanoneedles that stably exist in the solution (reddotted boxes in Figure 1e-g). This formation process of gypsum nanoneedles is schematically illustrated in Figure 1h, which highlights the direct aggregation pathway from smaller gypsum nanoparticles to larger gypsum nanoneedles. More tests were done to examine the beam effects, if any, in the aggregation process. As shown in Figure S2, similar phenomena were observed at a dose rate twice that of Figure 1. The stability of the aggregated gypsum nanoparticles was also tested under different beam-dose conditions. Without changes in the magnification, adjustment of the brightness can change the dose rate in the TEM mode. Changing the magnification can change the dose even more dramatically, as shown in Figure S3c, which shows a close-up of a large cluster. In this higher-dose case, the particles show a stable structure, with the aggregated gypsum remaining unchanged. This confirms the stability of the aggregated gypsum nanoparticles

ACS Applied Nano Materials Article

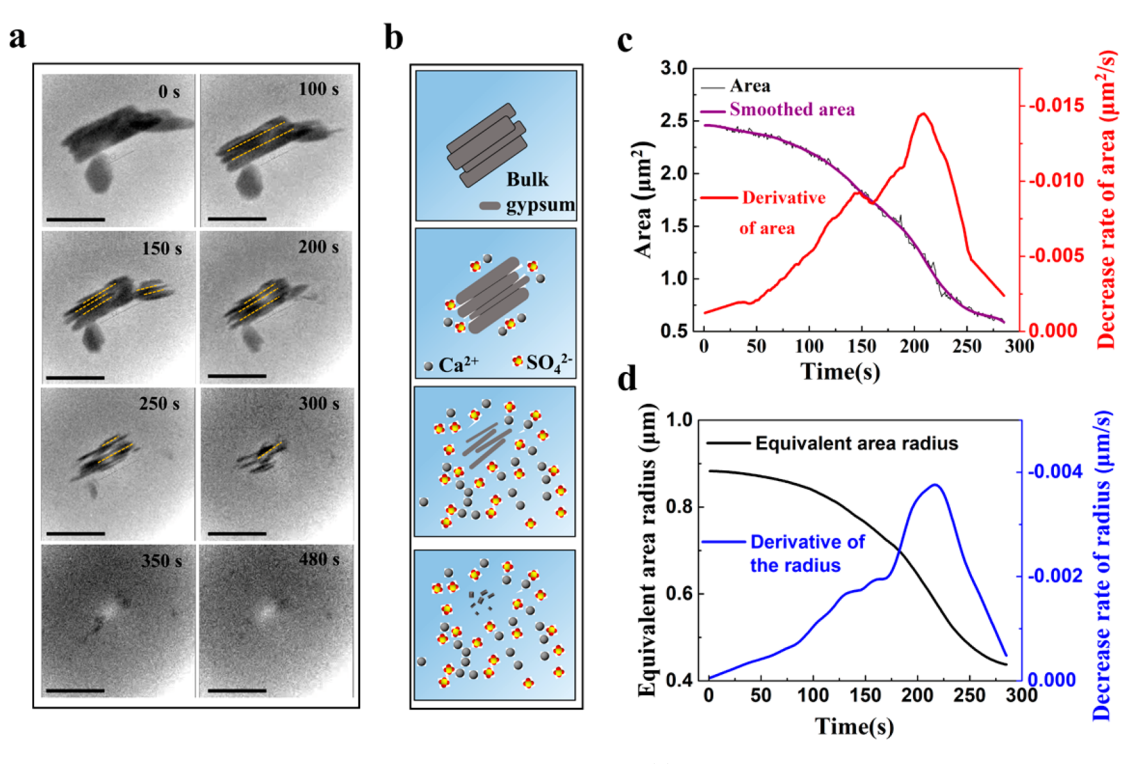


Figure 3. Dissolution of bulk gypsum in water observed via in situ liquid TEM. (a) Snapshots from Movie S2. The sequential images show the gradual dissolution of micron-sized bulk gypsum, which initiates from the attachment interfaces and surface cracks (marked by the yellow dashed lines). Scale bars denote 2 μ m, and the dose rate was 144 e nm⁻² s⁻¹. (b) Schematic showing the dissolution of bulk gypsum, with gray spheres indicating Ca²⁺ and yellow/red clusters indicating SO₄²⁻. (c) Measured projected area of the particle shown in part a with time (black line): smoothed curve (purple); first derivative of the smoothed curve (red). (d) Equivalent-area radius versus time (black) and its first derivative (blue).

under the electron beam (e-beam) for the conditions used here.

To further study the evolution of the formed gypsum nanoneedles in the solution, Figure 2a shows aggregated gypsum nanoparticles after 5 min of exposure in a SO₄²⁻- and Ca²⁺-saturated solution in a TEM cell that was not placed in the microscope chamber. The particles, after the timed exposure, were extracted from the cell and dried for immediate TEM imaging. The particles seem to be tightly clustered in a randomly oriented fashion, as marked by the blue dashed frames in Figure 2a. Figure 2b demonstrates the selected-area electron diffraction (SAED) pattern of the aggregated gypsum nanoparticles in Figure 2a; the rings can be indexed as the characteristic diffractions of polycrystalline gypsum, which is monoclinic in structure with crystalline planes of (041), (040), (111), etc. At a later stage, when the exposure time was increased to 30 min (Figure 2c,d), larger single-crystalline gypsum microneedles are seen to be well developed, with their growth direction normal to the (200) plane, as confirmed by the single-crystalline diffraction pattern in the inset of Figure 2d. Parts e and f of Figure 2 compare the histograms of the particle projected area after a 1 s exposure time (Figure 1b; in situ) and after 5 min exposure (Figure 2a; ex situ); during that period, the projected particle area grows to more than 0.05 μm^2 (area-equivalent diameter around 252 nm). In TEM imaging, the actual particle shape cannot be determined from the projected view. In the present test, most particles did not have regular shapes; thus, the area-equivalent diameter was used to describe the growth trend. The equivalent diameter was calculated from $d = 2\sqrt{A/\pi}$, where A is the projected area of each particle.²⁷ Most of the particles have projected areas up to 0.11 μ m² (equivalent diameter up to 374 nm with an

average of 160 nm) after 5 min exposure, while these values are $0.05 \ \mu \text{m}^2$ (diameter up to 252 nm with an average of 112 nm) after a 1 s exposure. This indicates that gypsum nanoparticles simply grow and aggregate via self-assembly in the initial stages. These findings strongly support the hypothesis that the gypsum nanoparticles (Figure 1b) can form gypsum nanoneedles (red dotted boxes in Figure 1e-g) partially assembled at the nanoscale. Figure 2a, which shows gypsum exposed for 5 min to a Ca²⁺- and SO₄²⁻-saturated aqueous solution, provides evidence of oriented attachment of the gypsum nanoparticles (highlighted by blue dash outlines). The corresponding SAED pattern shows polycrystalline features. At a later stage (e.g., Figure 2c, 30 min exposure), formation of the needle shape becomes obvious. The corresponding SAED pattern shows single-crystal spots (Figures 2d and S4). Some spots are not circular, showing obvious elongation. The SAED pattern shows some circular features. In the TEM images, some nanoparticles could be observed in single-crystalline gypsum nanoneedles (red ovals marked in Figure S4a). This indicates that the particle is not a perfect single crystal, but because different grains contribute to the SAED pattern, it is rather a quasi single crystal. The reconstructed red-green-blue (RGB) highresolution image of the gypsum needle also proves the orientation relationship among the red, blue, and green gypsum grains. It was seen that the three grains are assembled together. For the gypsum microneedles shown in Figure S7a, the dots in the SAED pattern are neat and clean, indicating a typical single crystal. This evolution of the SAED pattern from polycrystal to quasi-single-crystalline to neat single-crystalline character supports the self-assembly growth of gypsum needles. This in situ observation not only records the early aggregation of gypsum nanoparticles and the final formation of single-

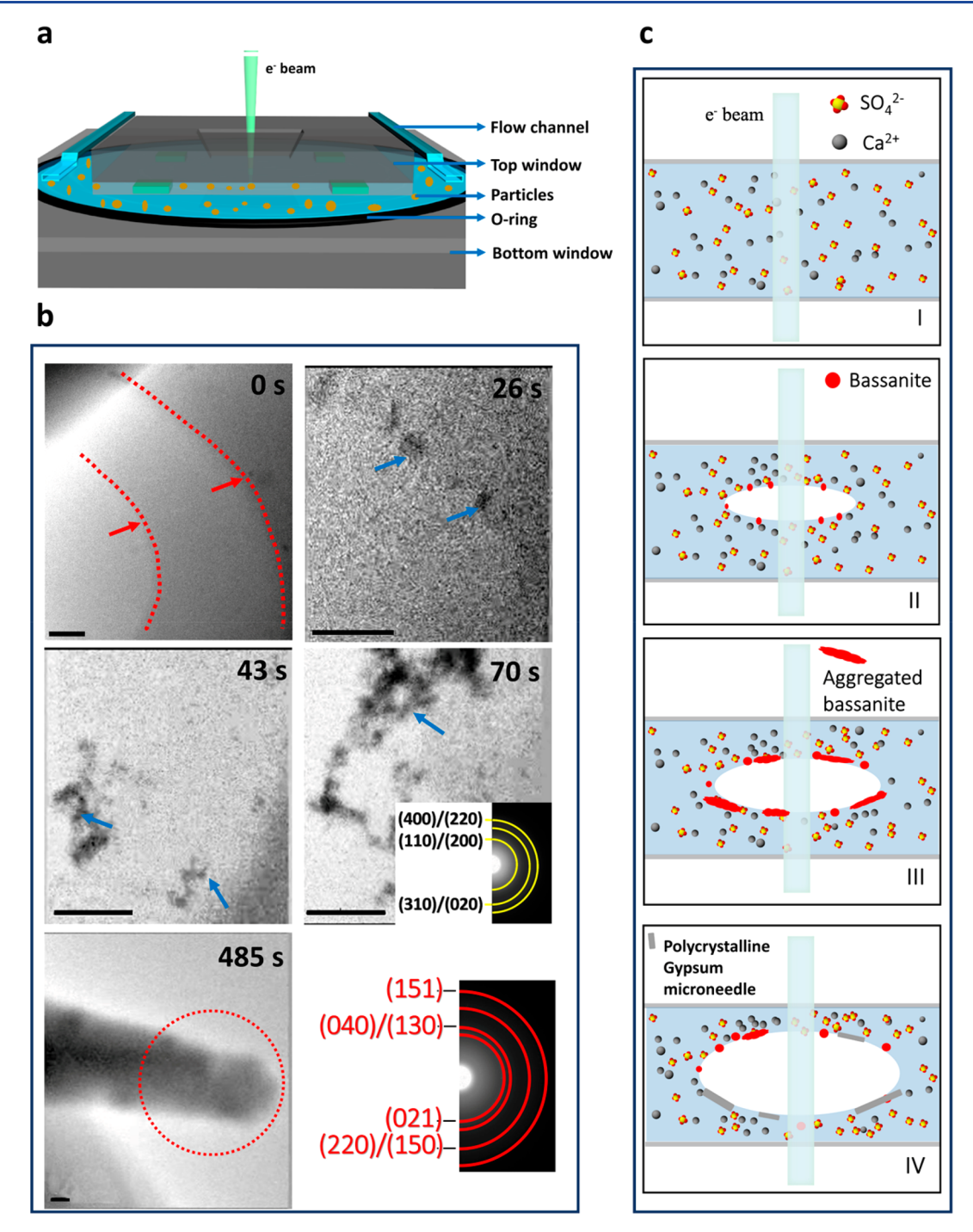


Figure 4. Precipitation of metastable bassanite and stable gypsum in a Ca^{2+} - and SO_4^{2-} -saturated solution. (a) Schematic of the liquid-cell TEM experimental setup in the flow mode. Only the top and bottom chips are shown for better depiction of the flow chamber. (b) Time-sequenced TEM images showing the dynamic process involving (0 s) bubble formation in the viewing area, (26 s) nascent bassanite nanoparticle nucleation near the bubble interface, (43 s) aggregation of bassanite nanoparticles, (70 s) assembly of bassanite nanoparticles toward the needle shape, and (485 s) a polycrystalline gypsum microneedle. The SAED patterns (insets in the respective frames) taken at 70 and 485 s confirm the existence of the bassanite and gypsum phases, respectively. Each scale bar in part b denotes 200 nm. The electron dose rate was 4413 e nm⁻² s⁻¹. (c) Schematics illustrating the four stages (I–IV) of gypsum formation within an unsaturated solution containing Ca^{2+} and SO_4^{2-} and which is irradiated by the condensed beam to induce phase change (bubble), which locally raises the concentration of the ions in the liquid and causes solid precipitation.

crystalline gypsum microneedles, but also confirms the compositions of the particles/needles involved in the whole process, where gypsum nanoparticles reorient themselves to form gypsum nanoneedles. This self-assembly growth mechanism has also been reported for other nanostructures during solution-based reactions, ^{36–38} where the driving force was

believed to be a reduction of the surface energy of the overall system. Thus, it appears that gypsum nanoparticles can form single-crystalline gypsum microneedles through aggregation and self-assembly, as long as a sufficient solution exposure time is guaranteed.

3.2. Dissolution of Bulk Gypsum in an Unsaturated Solution. After examining the behavior of gypsum nanoparticles immersed in a SO_4^{2-}/Ca^{2+} -saturated solution and demonstrating the growth mechanism via self-assembly, we explored situations where particles were immersed in an unsaturated solution with low SO_4^{2-}/Ca^{2+} concentration. Assisted by in situ liquid TEM, we investigated this case, and the results are shown in Figure 3 (Movie S2). After immersing pristine bulk gypsum in an unsaturated solution, instead of particle growth, we observed the gradual dissolution of gypsum with the subsequent release of SO_4^{2-} and Ca^{2+} into the solution, as well as the expected formation of aqueous complex CaSO₄(aq) (Table S1). From Figure 3a and Movie S2, one can see that the dissolution proceeds preferably along the interface regions (yellow dashed lines) between planar sections of the particle, thus creating cracks in the gypsum structure. With these interface regions being etched gradually, this larger particle goes through a disassembling process, which splits it into several gypsum nanoneedles. The schematic of this process is shown in Figure 3b. This observation within the unsaturated solution supports the hypothesis that the selfassembly of gypsum microneedles makes a significant contribution to the overall growth and formation of bulk gypsum. Figure S1c shows more examples of bulk gypsum particles involving obvious interface lines that imply the selfassembly growth process.

To quantify the kinetics of the growth/dissolution of gypsum, the relationship between the projected area of the particle and the time it is immersed in the solution is plotted in Figure 3c. The graph shows that while the particle area declines in time, dissolution proceeds slowly during the first 100 s, speeds up from 100 to about 200 s, and then slows shortly after 200 s. This interesting trend is clearly shown in the derivative curve (red), where the dissolution rate is initially small, then increases gradually to 0.015 μ m² s⁻¹ just beyond 200 s, and finally falls back to a low value after 250 s. Figure 3d shows the corresponding variation of the particle equivalent radius (based on the projected area) and its derivative. Because the concentration of the ions is not detectable in liquid-cell TEM, the sizes of the particles are used to provide a measure of the amount of ions in the liquid versus time. Dissolution of the gypsum particles could be divided into two steps: (1) the gypsum particles become solvated, followed by (2) diffusion of the dissolved ions into the solution. In this case, and before 200 s, the equivalent-area radius varies in a quadratic form with time, which supports the diffusion layer model.^{39,40} First, the gypsum dissolves in water to form a saturated ion layer, also known as the stagnant layer, 41 and then the ions diffuse into the solution. Because step 1 is faster than step 2, diffusion of the ions is the rate-determining factor. The Noyes-Whitney equation could thus describe this process. 42,43 After 200 s, the equivalent-area radius decreases according to a more complex r(t) form. From Figure 3a, it can be seen that bulk gypsum is almost dissolved and some small gypsum needles persist. In this test, the flow of water was stopped (closed system). As such, the concentration of the ions in water could have reached the saturation level, thus reducing the dissolution rate. Steps 1 and 2 became comparable in rate, meaning that neither interfacial dissolution nor ion diffusion is the limiting factor in this case.41

To examine the influence of the e-beam on the dissolution of gypsum, Figure S5 shows snapshots (from Movie S3) of another bulk gypsum particle floating around the gradually

dissolving particle shown in Figure 3. Although the gypsum particle in Figure S5 was exposed to the same electron dose, it remained intact from the beginning of the observation, with no obvious dissolution even after 900 s of beam exposure. This example indicates the stability of gypsum when subjected to ebeam imaging. Considering that the images in Figure S5 were captured several minutes after those in Figure 3, we expect that the surrounding solution had become saturated or nearsaturated by dissolving gypsum when the event in Figure 3 was recorded. The surrounding saturated solution then helped to stabilize the gypsum particle in Figure S5 and prevented its dissolution. In conclusion, the e-beam appears to have a limited effect on the real-time liquid TEM observation of the dissolution events examined herein.

3.3. Precipitation of Gypsum from an Unsaturated **Solution.** On the basis of the acquired understanding of interactions between the aqueous solution and the preexisting bulk gypsum in the solution, we further studied the kinetics of gypsum nucleation, precipitation, and growth when the solution was gradually saturated in real time. An unsaturated solution of Ca²⁺ and SO₄²⁻ was driven into the TEM cell through a microfluidic device (Figure 4a); there should be no gypsum precipitation at the beginning. To trigger gypsum nucleation in the unsaturated solution, the e-beam was focused on a small region of the solution to trigger bubble formation^{32,44} (red arrows mark the bubble interface in Figure 4b), by which a locally supersaturated solution was intentionally generated. It has been reported that radiolysis caused by the high-energy e-beam generates bubbles consisting of oxygen and hydrogen gases. 45 The gases in the bubble displace the surrounding solvent and thus increase the concentration of Ca^{2+} and SO_4^{2-} in the surrounding solution, in turn leading to the nucleation of new nanoparticles (blue arrows in Figure 4b; 26-70 s). The SAED pattern confirms that these precipitated nanoparticles consist of polycrystalline bassanite (the inset in Figure 4b; 70 s) with monoclinic structure. This agrees with previous reports that demonstrated the intermediate metastable bassanite during the synthesis of gypsum using either conventional TEM¹³ or cryo-TEM.¹⁴ Eventually, these bassanite nanoparticles are expected to go through a phase transition to aggregated gypsum polycrystalline microneedles (Figure 4b; 485 s). The dynamic precipitation and growth of gypsum microneedles, based on these observations, is schematically illustrated in Figure 4c. During the process, initially, bassanite nanoparticles precipitate from the Ca²⁺- and SO₄²-saturated solution. Next, these bassanite nanoparticles aggregate to form bassanite nanoclusters. After that, the bassanite nanoclusters transform (by hydration) to gypsum nanoneedles, which eventually form gypsum microneedles, as shown in Figure 2. Because tracking the whole process is difficult in the liquid cell, only part of this process was captured and is shown in Figure 4b.

3.4. Discussion. Although in the liquid cell the e-beam effects can be a main concern, we have concluded the e-beam effects are not significant in the present experiments. The dose rates for Figures 1, 3, and 4 were estimated to be 798, 144, and 4413 e nm⁻² s⁻¹, respectively. For gypsum aggregation in liquid (Figure 1), the flow mode of the liquid cell was used to minimize the e-beam effects in the local area. The flow rate was 300 $\mu L\ h^{-1}$, as determined from the liquid flow marked by the moving particles and the dimensions of the cell. Because of this liquid flow, the solution, after absorbing energy from the ebeam, moves out of the irradiated area. This effectively lowers

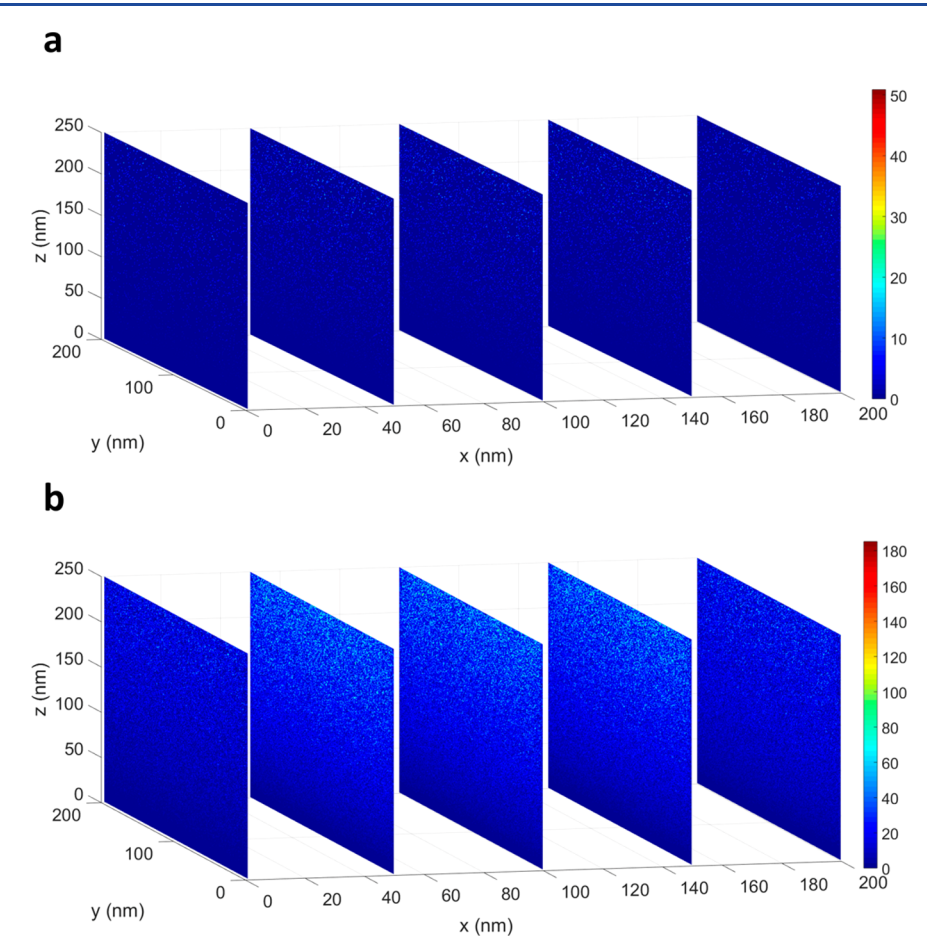


Figure 5. MC calculation of the energy delivered by an e-beam with (a) low dose $(144 \text{ e nm}^{-2} \text{ s}^{-1})$ and (b) high dose $(4413 \text{ e nm}^{-2} \text{ s}^{-1})$. Z is the liquid depth along the e-beam. The width and length of the simulated area are equal to 200 nm. The color scale bars denote eV nm⁻³.

the accumulated energy for the local area and raises the threshold for bubble formation. 46 Based on published work, 44,47-49 the critical dose rate for generating bubbles depends on the microscope parameters and the experimental setup. Wang et al. reported that the threshold dose rate for bubble formation in a static silicon nitride membrane liquid cell is 10 e nm⁻² s⁻¹ at 80 kV. 48 Grogan et al. 44 reported that bubbles could be generated in a static silicon nitride membrane liquid cell with a dose rate of around 792 e nm⁻² s⁻¹ at 300 kV. For the present work, with a 200 kV e-beam and the flowingliquid setting, the threshold dose for bubble generation should be higher than that reported for static cells. 44,48 So, for the gypsum particle aggregation test (Figure 1), the dose rate used is lower than the threshold for bubble formation. For the dissolution test (Figure 3), the dose rate is well below the threshold for bubble formation. For the precipitation test (Figure 4, where the dose rate is $4413 \text{ e nm}^{-2} \text{ s}^{-1}$), we used the static mode to generate a bubble. Other concerns about the ebeam effect stem from the physical and chemical environmental changes caused by the e-beam. For the physical aspect, temperature is a key point for most chemical reactions. The temperature difference is estimated to be less than 2 K, 50 thus making its effect negligible. For the chemical aspect, one should focus on the radicals generated by the e-beam. Hence, a Monte Carlo (MC) simulation was carried out to determine the density distribution in a 200×200 nm liquid area with 150 nm thickness. 51,52 On the basis of this simulation (Figures 5 and S8 and S9), for the low-dose case (144 e nm⁻² s⁻¹), there

are barely any radicals generated by the e-beam. For the highdose case (4413 e nm⁻² s⁻¹), the energy transferred to the liquid is higher than that for the low-dose case, while the average is still lower than 100 eV nm⁻³. More energy is delivered to the top area of the liquid cell compared to the bottom area for the high-dose case (Figure 5b). The dose would accumulate with time, but the steady-state concentrations of radicals are only dose-rate-related. 44,45 For hydrogen gas, the steady-state concentration is around 1 mM for the high dose in this test. 45 For other radicals, the concentration is between 0.1 and 0.01 mM, 45 which is also very low. Another obvious change caused by the e-beam is on the pH of the solution, which may approach 4.5 under prolonged e-beam irradiation.⁴⁵ On the basis of the Pourbaix diagram of the calcium system, calcium is stable for a wide range of pH values (1-12). So The dissolution 3,54 and precipitation 2,4,18 of gypsum are not pH-sensitive. SO_4^{2-} is a strong acid anion, which is stable with the Ca cation. So, generally, the pH change caused by the e-beam should not have a significant effect on the Ca/ SO₄ system. This means that, although the e-beam may alter the chemical environment of the liquid, the associated change is not sufficient enough to alter the outcome.

To further rationalize the proposed oriented-attachment mechanism and the existence of an intermediate bassanite phase during the growth of gypsum particles, some thermodynamic considerations are discussed in the following. The presence of intermediate hemihydrate bassanite as a precursor to gypsum formation in the CaSO₄ system is

ACS Applied Nano Materials Article

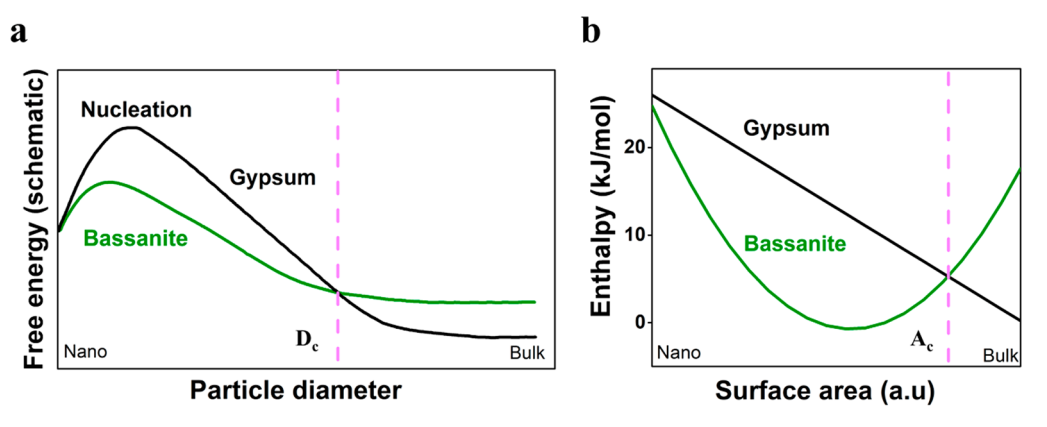


Figure 6. (a) Free energy of the two main hydrated forms of CaSO₄ as a function of the particle size.⁵⁵ Both axes have no specific units and demonstrate only the trends. (b) Enthalpy of the reaction of bassanite and gypsum versus particle surface area.¹⁴

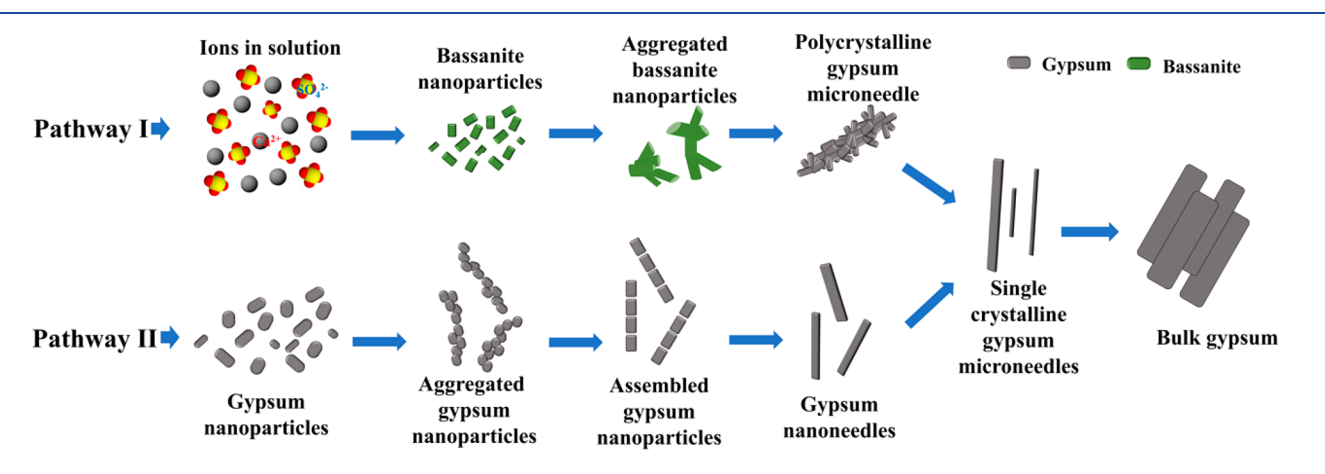


Figure 7. Schematic of two confirmed pathways for the formation of gypsum microneedles. In pathway I, bassanite nanoparticles precipitate from the solution saturated with Ca^{2+}/SO_4^{2-} ions and then grow via self-assembly to transform to polycrystalline gypsum microneedles, which finally grow to bulk gypsum. In pathway II, gypsum nanoparticles directly form gypsum microneedles via aggregation and assembly, and then form bulk gypsum.

consistent with the findings of Van Driessche et al., 14 who implied the crucial role of self-assembly in this phase transition. Thermodynamically, the solubility of the bassanite nanocrystals was hypothesized to be much smaller than that of bulk bassanite. Figure 6 (based on ref 42) displays the free energy and enthalpy of associated reactions involving bassanite and gypsum particles, as well as comparisons taking into consideration the particle size and surface area (which rises as the size declines). Figure 6a is not based on the present experimental results; it is derived from a general case for the energetics of metastable and stable polymorphs as a function of the particle radius.⁵⁵ However, the energy trend is similar to the present case, thus helping rationalize the energy barrier during the precipitation process. For bassanite and gypsum phases possessing a certain particle size, the phase with lower enthalpy and free energy would be more stable in solution and thus more likely to be captured in an experiment. Following this principle, bassanite is more stable than gypsum when the particle size is smaller than D_c , the critical diameter where the two curves cross over. The phenomena displayed in Figure 4b agree with the findings of Van Driessche et al. 14 However, it is important to note that, as the particle size decreases into the nanoscale regime (left side of the graphs in Figure 6), the enthalpies of bassanite and gypsum become comparable. In this regime, both bassanite and gypsum particles are thermodynamically stable, and thus both are likely to be

formed and observed experimentally, as shown in Figures 1, 2, and S4. In all of these figures, the as-formed particles fall into the nanoscale range. The sizes of the gypsum nanoparticles shown in Figures 1b and 2a are around 160 and 100 nm, respectively, and the sizes of the precipitated bassanite nanoparticles in Figure 4b increase from 38 nm at 26 s to 123 nm at 43 s to 347 nm at 70 s. The size of bassanite at a later stage where the phase transition of bassanite to gypsum happens is larger than 347 nm. So, on the basis of our experiments and other reports 13,14 (Table S2), D_c for the transition of bassanite to gypsum should fall in the range of 500 nm to 1 μ m. On the basis of the experimental data and calculations, 14 the evolution of the enthalpy of bassanite follows the green line in Figure 6b, and the crossover point between gypsum and bassanite (marked by a pink dashed line) should be near 0.25 μ m² (which corresponds to an equivalent size of ~500 nm). The formation energy for bassanite at the nanoscale level is lower than that for gypsum, 14 and it is thus easier to precipitate bassanite than gypsum (Figure 4). However, with the particle size increasing above D_c , as indicated by the crossover point of bassanite and gypsum in Figure 6, the gypsum phase possesses a lower energy than bassanite, so a bassanite-to-gypsum phase transition occurs. With a gradual increase of the particle size, bassanite can transform to gypsum. On the other hand, gypsum would not transform to bassanite (see the Supporting Information). In

other words, the gypsum particles can exist stably without phase transition even when the size is smaller than D_c . The initial size of the gypsum nanoparticles in our first experiment (Figure 1b-g, where particles were introduced in the cell) is much smaller than 500 nm, which supports that these (with a size smaller than D_c) gypsum nanoparticles can stably exist in solution. For all experiments in Figures 1 and 2, only the gypsum phase was involved, and no bassanite was detected. Driven by the trend of surface energy reduction, the orientedattachment mechanism gradually dominates the growth of gypsum nanoparticles to reduce the overall energy of the system. The gypsum microneedles can grow to bulk gypsum by oriented attachment along the direction [100] for this case, as deduced from SAED (insets in Figures 2d and S7). This is also consistent with the phenomena in Figure 2. On the basis of the discussion above, two possible pathways accounting for the formation of gypsum microneedles are supported here. One pathway is a conventional phase-transition-based mechanism involving the formation of an intermediate bassanite phase, as shown in Figures 4 and S7. The second pathway features direct gypsum growth without any intermediate phase, as demonstrated in Figure 1. Both mechanisms are illustrated in Figure 7.

In summary, two pathways for the growth of gypsum needles have been identified and explained (Figure 7). One pathway follows the conventional synthesis process of gypsum with bassanite acting as the intermediate phase. The new pathway discovered in this work is the direct self-assembly of gypsum nanoparticles to form gypsum microneedles, with no intermediate bassanite phase in the process. This pathway might offer a novel strategy to produce gypsum at industrial scales. Future industrial synthesis of gypsum can potentially realize significant energy savings and cost reduction by avoiding the calcination of ground gypsum. In addition, the present findings may lead to better strategies to avoid the unwanted contamination of equipment that operates in contact with water-dissolved CaSO₄. More perspective work is needed in the future to explore such growth mechanisms, so as to efficiently direct technological advancements toward the costeffective mass production of industrial products.

4. CONCLUSIONS

We have carried out dynamic in situ liquid TEM measurements of gypsum evolution from dry to hydrated states in real time and with nanoscale resolution. On the basis of these observations, two distinct pathways have been identified for formation of the well-known gypsum microneedles in an aqueous solution of CaSO₄. The first pathway agrees with an earlier-proposed mechanism starting from ions in the aqueous medium, where the nucleation of bassanite from Ca²⁺- and SO₄²⁻- saturated solutions is followed by further hydration to form gypsum microneedles. The second pathway, which has not been proposed before, features a dynamic self-assembled attachment growth mechanism, where randomly shaped gypsum nanoparticles aggregate and form gypsum microneedles in a Ca²⁺- and SO₄²-saturated solution. The present findings are supported by thermodynamic considerations, indicating that both bassanite and gypsum nanoparticles are equally stable in a saturated solution and thus could appear simultaneously to account for the formation of gypsum microneedles. This work could potentially revolutionize the gypsum industry by providing the foundation for a novel method to synthesize gypsum microneedles via nanoscale

processing rather than heat-induced phase transitions involving intermediate bassanite. As such, this potential industrial innovation, if scalable, could lead to energy- and time-efficient mass production of bulk gypsum for its wide applications in modern society.

ASSOCIATED CONTENT

S Supporting Information

The Supporting Information is available free of charge on the ACS Publications website at DOI: 10.1021/acsanm.8b00739.

Characterization of as-received gypsum powder, calculated species concentrations in saturated gypsum aqueous solution, in situ liquid-cell experiments showing stable gypsum particles in aqueous solutions, thermodynamic discussion, ex situ TEM characterization, TEM images of dried gypsum particles after immersion in water for different time periods, MC calculations of radicals generated by the e-beam, and a comparison of the gypsum and bassanite characteristic sizes at different conditions (PDF)

Accelerated video of gypsum particle aggregation in water (AVI)

Accelerated video of gypsum particle dissolution in water (AVI)

Accelerated video of a gypsum particle in water for 30 min (AVI)

Accelerated video of a particle precipitated from Ca²⁺and SO_4^{2-} -saturated aqueous solution subjected to strong beam irradiation, causing bubbling (AVI)

AUTHOR INFORMATION

Corresponding Authors

*E-mail: tolou@uic.edu. *E-mail: cmm@uic.edu. *E-mail: rsyassar@uic.edu.

Anmin Nie: 0000-0002-0180-1366

Seyed Mohammadreza Ghodsi: 0000-0002-7546-1253

Boao Song: 0000-0003-3124-3235 Jun Lu: 0000-0003-0858-8577

Constantine M. Megaridis: 0000-0002-6339-6933 Reza Shahbazian-Yassar: 0000-0002-7744-4780

Author Contributions

K.H. and all corresponding authors conceived the idea and discussed the detailed experimental design. K.H. ran the in situ liquid TEM experiments. K.H., A.N., Y.Y., and S.M.G. performed the ex situ TEM experiments and assisted with the in situ TEM experiments. E.F. ran the MC simulation. K.H. and Y.Y. wrote the manuscript under the direction of R.S.-Y., T.S., and C.M.M. Finally, B.S. and E.F. helped with some manuscript tasks.

Notes

1

The authors declare no competing financial interest.

ACKNOWLEDGMENTS

The work was conducted with partial financial support from USG. T.S.H. and R.S.-Y. acknowledge funding from NSF Award DMR-1710049. The research made use of instruments in the Electron Microscopy Service of the UIC Research Resources Center. Acquisition of the UIC JEOL JEM-ARM200CF was supported by an MRI-R2 grant from NSF

(Award DMR-0959470). The authors thank Dr. Kumar Natesaiyer of USG for useful discussions. J.L. gratefully acknowledges support from the U. S. Department of Energy (DOE), Office of Energy Efficiency and Renewable Energy, Vehicle Technologies Office. Argonne National Laboratory is operated for DOE Office of Science by UChicago Argonne, LLC, under contract number DE-AC02-06CH11357. Support to K.H. from a China Scholarship Council award is also acknowledged.

REFERENCES

- (1) Eckardt, F. D.; Spiro, B. The Origin of Sulphur in Gypsum and Dissolved Sulphate in the Central Namib Desert, Namibia. *Sediment. Geol.* **1999**, *123*, 255–273.
- (2) Gomis-Yagües, V.; Boluda-Botella, N.; Ruiz-Beviá, F. Gypsum Precipitation/Dissolution as an Explanation of the Decrease of Sulphate Concentration during Seawater Intrusion. *J. Hydrol.* **2000**, 228, 48–55.
- (3) Raines, M. A.; Dewers, T. A. Mixed Transport/Reaction Control of Gypsum Dissolution Kinetics in Aqueous Solutions and Initiation of Gypsum Karst. *Chem. Geol.* **1997**, *140*, 29–48.
- (4) Thompson, J.; Ferris, F. Cyanobacterial Precipitation of Gypsum, Calcite, and Magnesite from Natural Alkaline Lake Water. *Geology* **1990**, *18*, 995–998.
- (5) Medina-Elizalde, M.; Rohling, E. J. Collapse of Classic Maya Civilization Related to Modest Reduction in Precipitation. *Science* **2012**, 335, 956–959.
- (6) Barnett, W. K. Optical Petrography as a Tool for Examining Gypsum and Lime Plaster Pyrotechnology. *J. Field Archaeol.* **1991**, *18*, 253–255.
- (7) Sohmura, T.; Wakabayashi, K.; Lowmunkong, R.; Hojo, H.; Kusumoto, N.; Okuda, H.; Kojima, T.; Nakamura, T.; Yatani, H.; Takahashi, J. 3D Shape Measurement of Dental Casts Using Medical X-ray CT. *Dent. Mater. J.* **2004**, 23, 121–128.
- (8) Weeks, K.; Fraass, B.; Hutchins, K. Gypsum Mixtures for Compensator Construction. *Med. Phys.* **1988**, *15*, 410–414.
- (9) Tian, B.; Cohen, M. D. Does Gypsum Formation During Sulfate Attack on Concrete Lead to Expansion? *Cem. Concr. Res.* **2000**, *30*, 117–123.
- (10) Schossig, P.; Henning, H.-M.; Gschwander, S.; Haussmann, T. Micro-encapsulated Phase-change Materials Integrated into Construction Materials. *Sol. Energy Mater. Sol. Cells* **2005**, *89*, 297–306.
- (11) Karni, J.; Karni, E. Y. Gypsum in Construction: Origin and Properties. *Mater. Constr.* 1995, 28, 92–100.
- (12) Kusumoto, N.; Sohmura, T.; Yamada, S.; Wakabayashi, K.; Nakamura, T.; Yatani, H. Application of Virtual Reality Force Feedback Haptic Device for Oral Implant Surgery. *Clin. Oral Implants Res.* **2006**, *17*, 708–713.
- (13) Wang, Y.-W.; Kim, Y.-Y.; Christenson, H. K.; Meldrum, F. C. A New Precipitation Pathway for Calcium Sulfate Dihydrate (Gypsum) via Amorphous and Hemihydrate Intermediates. *Chem. Commun.* **2012**, *48*, 504–506.
- (14) Van Driessche, A.; Benning, L.; Rodriguez-Blanco, J.; Ossorio, M.; Bots, P.; García-Ruiz, J. The Role and Implications of Bassanite as a Stable Precursor Phase to Gypsum Precipitation. *Science* **2012**, 336, 69–72.
- (15) Eberl, J. J.; Ingram, A. R. Process for Making High-strength Plaster of Paris. *Ind. Eng. Chem.* **1949**, *41*, 1061–1065.
- (16) Manning, D. A.; Decleer, J. Introduction to Industrial Minerals, 1st ed.; Springer: New York, 1995; pp 141–158.
- (17) Corselli, C.; Aghib, F. S. Brine Formation and Gypsum Precipitation in the Bannock Basin, Eastern Mediterranean. *Mar. Geol.* **1987**, 75, 185–199.
- (18) Seewoo, S.; Van Hille, R.; Lewis, A. Aspects of Gypsum Precipitation in Scaling Waters. *Hydrometallurgy* **2004**, *75*, 135–146.
- (19) Saha, A.; Lee, J.; Pancera, S. M.; Bräeu, M. F.; Kempter, A.; Tripathi, A.; Bose, A. New Insights into the Transformation of Calcium Sulfate Hemihydrate to Gypsum Using Time-resolved

Cryogenic Transmission Electron Microscopy. Langmuir 2012, 28, 11182–11187.

Article

- (20) Stawski, T. M.; Van Driessche, A. E.; Ossorio, M.; Diego Rodriguez-Blanco, J.; Besselink, R.; Benning, L. G. Formation of Calcium Sulfate Through the Aggregation of Sub-3 nanometre Primary Species. *Nat. Commun.* **2016**, *7*, 11177.
- (21) Stach, R.; Krebs, P.; Jones, F.; Mizaikoff, B. Observing Nonclassical Crystallisation Processes in Gypsum via Infrared Attenuated Total Reflectance Spectroscopy. CrystEngComm 2017, 19, 14–17.
- (22) Prieto-Taboada, N.; Gómez-Laserna, O.; Martínez-Arkarazo, I.; Olazabal, M. Á.; Madariaga, J. M. Raman Spectra of the Different Phases in the CaSO₄–H₂O System. *Anal. Chem.* **2014**, *86*, 10131–10137.
- (23) Li, Y.; Sadakata, M. Study of Gypsum Formation for Appropriate Dry Desulfurization Process of Flue Gas. *Fuel* **1999**, 78, 1089–1095.
- (24) Shih, W.-Y.; Rahardianto, A.; Lee, R.-W.; Cohen, Y. Morphometric Characterization of Calcium Sulfate Dihydrate (Gypsum) Scale on Reverse Osmosis Membranes. *J. Membr. Sci.* **2005**, 252, 253–263.
- (25) Fan, C.; Teng, H. H. Surface Behavior of Gypsum During Dissolution. Chem. Geol. 2007, 245, 242-253.
- (26) Woehl, T. J.; Park, C.; Evans, J. E.; Arslan, I.; Ristenpart, W. D.; Browning, N. D. Direct Observation of Aggregative Nanoparticle Growth: Kinetic Modeling of the Size Distribution and Growth Rate. *Nano Lett.* **2014**, *14*, 373–378.
- (27) Zheng, H.; Smith, R. K.; Jun, Y.-w.; Kisielowski, C.; Dahmen, U.; Alivisatos, A. P. Observation of Single Colloidal Platinum Nanocrystal Growth Trajectories. *Science* **2009**, 324, 1309–1312.
- (28) De Jonge, N.; Peckys, D. B.; Kremers, G.; Piston, D. Electron Microscopy of Whole Cells in Liquid with Nanometer Resolution. *Proc. Natl. Acad. Sci. U. S. A.* **2009**, *106*, 2159–2164.
- (29) Williamson, M.; Tromp, R.; Vereecken, P.; Hull, R.; Ross, F. Dynamic Microscopy of Nanoscale Cluster Growth at the Solidliquid Interface. *Nat. Mater.* **2003**, *2*, 532–536.
- (30) Holtz, M. E.; Yu, Y.; Gunceler, D.; Gao, J.; Sundararaman, R.; Schwarz, K. A.; Arias, T. A.; Abruna, H. D.; Muller, D. A. Nanoscale Imaging of Lithium Ion Distribution During in Situ Operation of Battery Electrode and Electrolyte. *Nano Lett.* **2014**, *14*, 1453–9.
- (31) Xin, H. L.; Zheng, H. In Situ Observation of Oscillatory Growth of Bismuth Nanoparticles. *Nano Lett.* **2012**, *12*, 1470–1474.
- (32) Kraus, T.; de Jonge, N. Dendritic Gold Nanowire Growth Observed in Liquid with Transmission Electron Microscopy. *Langmuir* **2013**, 29, 8427–32.
- (33) Song, B.; He, K.; Yuan, Y.; Sharifi-Asl, S.; Cheng, M.; Lu, J.; Saidi, W. A.; Shahbazian Yassar, R. In Situ Study of Nucleation and Growth Dynamics of Au Nanoparticles on MoS₂ Nanoflakes. *Nanoscale* **2018**, *10*, 15809.
- (34) He, K.; Bi, X.; Yuan, Y.; Foroozan, T.; Song, B.; Amine, K.; Lu, J.; Shahbazian-Yassar, R. Operando Liquid Cell Electron Microscopy of Discharge and Charge Kinetics in Lithium-oxygen Batteries. *Nano Energy* **2018**, *49*, 338–345.
- (35) Mehdi, B. L.; Qian, J.; Nasybulin, E.; Park, C.; Welch, D. A.; Faller, R.; Mehta, H.; Henderson, W. A.; Xu, W.; Wang, C. M.; Evans, J. E.; Liu, J.; Zhang, J.-G.; Mueller, K. T.; Browning, N. D. Observation and Quantification of Nanoscale Processes in Lithium Batteries by Operando Electrochemical (S) TEM. *Nano Lett.* **2015**, *15*, 2168–2173.
- (36) Zhang, J.; Huang, F.; Lin, Z. Progress of Nanocrystalline Growth Kinetics Based on Oriented Attachment. *Nanoscale* **2010**, *2*, 18–34.
- (37) Penn, R. L.; Banfield, J. F. Imperfect Oriented Attachment: Dislocation Generation in Defect-free Nanocrystals. *Science* **1998**, 281, 969–971.
- (38) Yuan, Y.; Wood, S. M.; He, K.; Yao, W.; Tompsett, D.; Lu, J.; Nie, A.; Islam, M. S.; Shahbazian-Yassar, R. Atomistic Insights into the Oriented Attachment of Tunnel-Based Oxide Nanostructures. *ACS Nano* **2016**, *10*, 539–548.

J

- (39) Higuchi, W. I. Diffusional Models Useful in Biopharmaceutics. Drug Release Rate Processes. *J. Pharm. Sci.* **1967**, *56*, 315–324.
- (40) Singhvi, G.; Singh, M. In-vitro Drug Release Characterization Models. *Int. J. Pharm. Stud. Res.* **2011**, *2*, 77–84.
- (41) Qiu, Y. Dissolution Mechanisms: Theoretical and Experimental Investigations. Thesis, University of Iowa, Ames, IA, 2015.
- (42) Noyes, A. A.; Whitney, W. R. The Rate of Solution of Solid Substances in their Own Solutions. *J. Am. Chem. Soc.* **1897**, *19*, 930–934
- (43) Lifshitz, I. M.; Slyozov, V. V. The Kinetics of Precipitation from Supersaturated Solid Solutions. *J. Phys. Chem. Solids* **1961**, *19*, 35–50.
- (44) Grogan, J. M.; Schneider, N. M.; Ross, F. M.; Bau, H. H. Bubble and Pattern Formation in Liquid Induced by an Electron Beam. *Nano Lett.* **2014**, *14*, 359–364.
- (45) Schneider, N. M.; Norton, M. M.; Mendel, B. J.; Grogan, J. M.; Ross, F. M.; Bau, H. H. Electron—Water Interactions and Implications for Liquid Cell Electron Microscopy. *J. Phys. Chem. C* **2014**, *118*, 22373—22382.
- (46) Ring, E. A.; De Jonge, N. Microfluidic System for Transmission Electron Microscopy. *Microsc. Microanal.* **2010**, *16*, 622–629.
- (47) Wang, C.; Qiao, Q.; Shokuhfar, T.; Klie, R. F. High-Resolution Electron Microscopy and Spectroscopy of Ferritin in Biocompatible Graphene Liquid Cells and Graphene Sandwiches. *Adv. Mater.* **2014**, 26, 3410–3414.
- (48) Wang, C.; Shokuhfar, T.; Klie, R. F. Precise In Situ Modulation of Local Liquid Chemistry via Electron Irradiation in Nanoreactors Based on Graphene Liquid Cells. *Adv. Mater.* **2016**, *28*, 7716–7722.
- (49) Shin, D.; Park, J. B.; Kim, Y.-J.; Kim, S. J.; Kang, J. H.; Lee, B.; Cho, S.-P.; Hong, B. H.; Novoselov, K. S. Growth Dynamics and Gas Transport Mechanism of Nanobubbles in Graphene Liquid Cells. *Nat. Commun.* **2015**, *6*, 6068.
- (50) Mirsaidov, U. M.; Zheng, H.; Bhattacharya, D.; Casana, Y.; Matsudaira, P. Direct Observation of Stick-slip Movements of Water Nanodroplets Induced by an Electron Beam. *Proc. Natl. Acad. Sci. U. S. A.* **2012**, *109*, 7187–7190.
- (51) Wang, Y.; Firlar, E.; Dai, X.; Libera, M. Poly(ethylene glycol) as a Biointeractive Electron-beam Resist. *J. Polym. Sci., Part B: Polym. Phys.* **2013**, *51*, 1543–1554.
- (52) Joy, D. C. Monte Carlo Modeling for Electron Microscopy and Microanalysis; Oxford University Press, 1995.
- (53) Takeno, N. Atlas of E_h-pH diagrams. Geological Survey of Japan Open File Report; 2005; Vol. 419, p 102.
- (54) Gabrisova, A.; Havlica, J.; Sahu, S. Stability of Calcium Sulphoaluminate Hydrates in Water Solutions with Various pH Values. *Cem. Concr. Res.* **1991**, *21*, 1023–1027.
- (55) Navrotsky, A. Energetic Clues to Pathways to Biomineralization: Precursors, Clusters, and Nanoparticles. *Proc. Natl. Acad. Sci. U. S. A.* **2004**, *101*, 12096–12101.
- (56) Viedma, C.; Cuccia, L. A.; McTaggart, A.; Kahr, B.; Martin, A. T.; McBride, J. M.; Cintas, P. Oriented Attachment by Enantioselective Facet Recognition in Millimeter-sized Gypsum Crystals. *Chem. Commun.* **2016**, *52*, 11673–11676.